Predicted detection rates of regional-scale meteorite impacts on Mars with the InSight short-period seismometer

N. A. Teanby[a]

[a]*School of Earth Sciences, University of Bristol, Wills Memorial Building, Queen's Road, Bristol, BS8 1RJ, U.K.*

Abstract

In 2016 NASA will launch the InSight discovery-class mission, which aims to study the detailed internal structure of Mars for the first time. Short- and long-period seismometers form a major component of InSight's payload and have the potential to detect seismic waves generated by meteorite impacts. Large globally detectable impact events producing craters with diameters of ∼100 m have been investigated previously and are likely to be rare (Teanby and Wookey, 2011), but smaller impacts producing craters in the 0.5–20 m range are more numerous and potentially occur sufficiently often to be detectable on regional scales ($\lesssim$1000 km). At these distances, seismic waves will have significant high frequency content and will be suited to detection with InSight's short-period seismometer SEIS-SP. In this paper I estimate the current martian crater production function from observations of new craters (Malin et al., 2006; Daubar et al., 2013), model results (Williams et al., 2014), and standard isochrons (Hartmann, 2005). These impact rates are combined with an empirical relation between impact energy, source-receiver

Email address: n.teanby@bristol.ac.uk (N. A. Teanby)

distance, and peak seismogram amplitude, derived from a compilation of seismic recordings of terrestrial and lunar impacts, chemical explosions, and nuclear tests. The resulting peak seismogram amplitude scaling law contains significant uncertainty, but can be used to predict impact detection rates. I estimate that for a short-period instrument, with a noise spectral density of 10^{-8} $ms^{-2}Hz^{-1/2}$ in the 1–16 Hz frequency band, approximately 0.1–30 regional impacts per year should be detectable with a nominal value of 1–3 impacts per year. Therefore, small regional impacts are likely to be a viable source of seismic energy for probing Mars' crustal and upper mantle structure. This is particularly appealing as such impacts should be easily located with orbital imagery, increasing their scientific value compared to other types of events with unknown origins. Finally, comparison of the empirical results presented here with the modelling study of Teanby and Wookey (2011) provides constraints on the seismic efficiency, suggesting that values of $\sim 5 \times 10^{-4}$ may be appropriate for impact generated seismic waves. Comparing explosion and impact datasets indicate that buried explosions are $\sim$10 times more efficient at generating seismic waves than impacts.

Keywords: Mars, Seismology, Impacts, InSight, craters

---

1. Introduction

Planetary interiors have the potential to tell us a great deal about planet formation and evolution, but remain one of the great unknown frontiers in Solar System research. Currently Mars' deep internal structure is constrained by observations of moment of inertia (Yoder et al., 2003; Sohl et al., 2005), composition estimates based on martian meteorites (Sohl and Spohn, 1997;

Zharkov and Gudkova, 2005), tidal dissipation inferred from the secular acceleration of Phobos (Zharkov and Gudkova, 1997), and inferences based on the absence of a large-scale global magnetic field (Acuna et al., 1999; Connerney et al., 1999). These observations do not uniquely constrain the internal structure and large uncertainties remain in fundamental properties such as core size and composition. Closer to the surface, Mars' relative crustal thickness is constrained by topography and gravity data (Zuber, 2001), but this also contains large uncertainties and relies on assumptions about crust-mantle density contrasts.

The most effective way to probe a planet's internal structure is using seismology (Shearer, 2009), which is challenging for space missions as it requires surface deployments (Anderson et al., 1976; Lognonne et al., 2000; Lorenz, 2012). Because of this, only Earth and the Moon currently have any reliable seismic data. The Viking 2 seismometer did successfully return data, but only one potential event was identified, which could have been caused by wind noise due to the instrument's unfavourable positioning on the lander deck. Seismology on Mars will extend our knowledge to an intermediate sized planet. This motivated NASA's Interior Exploration using Seismic Investigations, Geodesy and Heat Transport mission (InSight), which aims to probe the detailed internal structure of Mars. InSight is due to launch in March 2016 and will land on Mars in September 2016, with a nominal mission length of one Mars year.

The InSight seismometer package, SEIS, comprises two separate three-axis seismometers: a short-period seismometer SEIS-SP (Pike et al., 2005; Delahunty and Pike, 2014) designed to investigate frequencies above 0.1 Hz;

and a very broad band seismometer SEIS-VBB (Lognonne et al., 2014; Dandonneau et al., 2013) designed to investigate frequencies below 1 Hz. SEIS-SP has a sample rate of 100 Hz and SEIS-VBB has a sample rate of 20 Hz. Both seismometers will be mounted on a tripod that will be transferred to the surface with a robot arm and protected from wind and extreme temperature variations with a wind and thermal shield.

The two complementary seismometers will be suited to studying different types of seismic event, distinguished primarily by the frequency content of incoming seismic waves. Frequency content of seismic signals is dependent upon the source mechanism, with larger events having a lower source spectrum corner frequency (Shearer, 2009). There is also a dependence on source-receiver distance, as higher seismic frequencies are preferentially attenuated during wave propagation, meaning that much of the high frequency content is removed from distant events. SEIS-SP has peak sensitivity to high frequencies so will be most sensitive to local and regional seismic events, whereas SEIS-VBB has peak sensitivity to low seismic frequencies so will be most sensitive to teleseismic global events.

InSight's seismometers will rely on Mars being seismically active to probe the crustal and deep internal structure, so it is important to understand the kinds of sources that are likely to be active and the level of that activity. The two most important sources are expected to be faulting due to release of crustal stress and meteorite impacts.

Faulting is expected to be the most significant of these sources. Compelling evidence that faulting is still active today is provided by the fresh boulder trails observed on large graben structures, which are interpreted as

being caused by boulders released by seismic ground shaking (Roberts et al., 2012). Active faulting is also predicted from models that distribute stress release from long-term cooling over the global fault population (Knapmeyer et al., 2006), extrapolations from observed fault slips in units of different geological ages (Golombek et al., 1992), and most recently from graben slip rates determined from crater counting and high resolution topographic models (Taylor et al., 2013). However, the rate of seismicity is extremely uncertain as it depends critically on the strength of the martian crust, which is not well constrained. As a result, the estimated number of seismic events of a given magnitude occurring per year spans five orders of magnitude (Taylor et al., 2013). A fault source is also relatively complex and will be challenging to fully characterise with a single seismic station (Panning et al., 2015) - the depth, strike, and dip of the fault will all be unknown.

Meteorite impacts generate seismic energy during crater formation and provide a second type of seismic source. Impacts have the advantage that the seismic source is relatively simple, with an isotropic source function and a surface location. It may also be possible to locate impacts using orbital imagery, providing additional constraints. New impact craters have indeed been observed in high resolution orbital images from both Mars Global Surveyor (MGS) (Malin et al., 2006) and Mars Reconnaissance Orbiter (MRO) (Daubar et al., 2013, 2015). Impacts were also a significant seismic source on the Moon (Oberst and Nakamura, 1987; Gudkova et al., 2011), where many small impacts were detected because of the low seismic noise and lack of atmosphere to ablate and decelerate incoming material. On Earth, meteorite impacts are not a significant seismic source as most are ablated by the thick

atmosphere or obscured by high ambient noise levels. Direct seismic waves have only been detected from one natural impact event so far (Brown et al., 2008; Le Pichon et al., 2008; Tancredi et al., 2009), although seismic recordings of airbursts are more common (Edwards et al., 2008), either as a direct airwave or a ground-coupled airwave. Mars' thin atmosphere means that all but the smallest impactors should reach the surface, although they will be affected by ablation, deceleration, and fragmentation processes (Popova et al., 2003; Williams et al., 2014). These processes cause a deficiency in the number of small craters ($\ll$5 m diameter) compared to airless bodies like the Moon. However, such small craters will be very difficult to detect from orbit and are unlikely to generate detectable seismic waves over any significant distance.

Previous studies have focused on large globally detectable impact events (Davis, 1993; Teanby and Wookey, 2011). Davis (1993) uses a scaling of the lunar results and concluded that around 20 events should be globally detectable per year. However, Hartmann (2005) showed the current martian impact rate is in fact a lot lower than assumed by Davis (1993). More recently, Teanby and Wookey (2011) used updated estimates of the impactor population (Hartmann, 2005; Malin et al., 2006) and seismic waveform modelling to predict only one globally detectable event every 10 years. However, the results were strongly dependent on the seismic efficiency, which is very poorly constrained (Schultz and Gault, 1975; Richardson et al., 2005; Teanby and Wookey, 2011) and introduces uncertainties of at least an order of magnitude. In any case, large, globally detectable, impact events are likely to be rare, with a rate of about one event per year if we are optimistic about the

seismic efficiency. These distant large impacts will have undergone significant high frequency attenuation and will be best studied using SEIS-VBB (Lognonne et al., 2014).

The paucity of large global impact events motivates the work presented here. Small impacts are much more numerous (Hartmann, 2005; Malin et al., 2006; Daubar et al., 2013), but provide a much weaker seismic source, meaning that they may only be detectable regionally, which will require the seismometer to be located in close proximity to the impact site. These events will retain much of their high frequencies and be well suited to an investigation using SEIS-SP. At such close source-receiver distances, these events will be of limited use for studying the martian deep interior and core size. However, they will be extremely useful for studying crustal and upper mantle structure on regional scales.

Here I consider the detectability of small impacts based on estimates of the current crater production function and the InSight SEIS-SP seismometer specification. The approach is necessarily different to that in Teanby and Wookey (2011); full waveform modelling of local/regional small impacts is computationally unfeasible as it would require modelling of high seismic frequencies. Such modelling would also be dependent on crustal model assumptions, which contain large uncertainties and are likely to be highly variable. Instead, analogue terrestrial and lunar data from impacts and explosions are used to empirically determine signal levels and associated uncertainties for a given impact event.

Section 2 compiles updated estimates of the current crater production function based on recent new crater detections. Section 3 determines the

relation between impact energy, source-receiver distance, and seismic ground velocity for a wide range of crustal settings. Section 4 then develops a scaling relation between crater size and detection range, which is used to predict the number of events that could be detected with InSight's SEIS-SP instrument. Implications and limitations of the analyses are considered in Section 5

2. Current Crater Production Function

The current crater production rate on Mars can be defined in terms of isochrons. Throughout this study I follow Hartmann (2005)'s definition of an isochron, which is the incremental number of new craters in a given diameter range (or bin) created in a specified time interval. Conventionally, the bin centres are spaced equally in logarithmic space by a factor of $\sqrt{2}$, so that a bin centred on crater diameter D includes craters with diameters from $2^{-1/4}D$ to $2^{1/4}D$. Hartmann (2005) determined the crater production isochrons for Mars over geological timescales based on extrapolations from dated lunar samples. Subsequently, high resolution orbital imaging campaigns have discovered many new impact sites (Malin et al., 2006; Daubar et al., 2013, 2015), which provide an independent measure of the current cratering rate. New impact sites are typically first identified as low-albedo impact streaks in dusty areas, interpreted as clearing of higher albedo surface dust by the impact blast. These dark streaks are much easier to identify than craters alone, as they are much larger and are easily identified in single images. Once a potential new impact site is identified, repeat images (if available) can be used to check if the crater is indeed new. For this reason, most new impact site discoveries have been restricted to dusty regions.

Malin et al. (2006) used wide angle Mars Orbiter Camera (MOC) images from MGS with a resolution of 230 m/pixel to search for dark spots from new impacts. Follow up images were taken with the narrow angle camera at a resolution of 1.5 m/pixel. This allowed 20 new impact sites to be identified, which had crater diameters from 2–148 m. However, the largest 148 m crater is now suspected to be much older as aeolian bedforms are visible in crater bottom (Daubar et al., 2013). More recently Daubar et al. (2013) used MRO Context Camera (CTX) images with resolutions of 6 m/pixel combined with images from Viking, Mars Odyssey, Mars Express, MGS, and MRO to search for potential new impact sites. From these, 248 impacts sites were confirmed as new following inspection of 0.25 m/pixel High Resolution Imaging Science Experiment (HiRISE) images from MRO. A subset of 44 sites were particularly well constrained as they had both before and after CTX images. Crater diameters of 1.7–34 m were measured for this subset using HiRISE images (Daubar et al., 2013, theirTable 1).

Note that fragmentation in Mars' atmosphere often causes clusters of impact craters at a given impact site (e.g. Popova et al., 2003). The diameters reported by both Malin et al. (2006) and Daubar et al. (2013) are in terms of the so-called "effective diameter" D_{eff}, which represents an equivalent single crater diameter that would be created if no fragmentation occurred. D_{eff} is defined by:

$$D_{eff} = \left(\sum_{i=1}^{n} D_i^3 \right)^{1/3} \quad (1)$$

for a cluster with n individual craters with diameters D_i. Throughout the rest of this study I treat clusters of craters as a single crater with the effective

diameter. However, Daubar et al. (2013) report that 56% of new impact sites comprise crater clusters. The effect of this on potential impact-generated seismic signals is considered further in Section 5.

The new crater observations studies show that smaller craters are generally more numerous, as expected from the isochrons and crater populations. However, at the very smallest diameters, both Malin et al. (2006) and Daubar et al. (2013) observe a reduction in the number of small craters, which begins at $\sim$10 m in the Malin et al. (2006) study and $\sim$5 m in the Daubar et al. (2013) study. This downturn has two possible origins: atmospheric ablation removing the smallest impactors (Popova et al., 2003; Williams et al., 2014); or detection biases due to finite image resolution, which makes smaller craters more difficult to detect. Popova et al. (2003) predict that atmospheric effects should cause a downturn in small craters beginning at around 5 m, but more recent modelling by Williams et al. (2014) place the downturn at a crater diameter of around 0.2 m. As the CTX image resolution used to detect the new impacts is 6 m/pixel it is not possible to tell if the downturn at small diameters observed by Daubar et al. (2013) is due to atmospheric effects or finite image resolution. However, very high resolution HiRISE crater counts at Zunil crater by Williams et al. (2014) have a downturn starting around 1–2 m, comparable to the minimum crater size detectable with HiRISE, suggesting that atmospheric effects do not significantly reduce small cratering events until the sub-metre scale or below.

The new craters observations are now used to estimate present-day crater production functions. First, the new craters reported in Daubar et al. (2013) (their Table 1) and Malin et al. (2006) (their Table S1) are binned into

the same $\sqrt{2}$ crater diameter bins as Hartmann (2005). Second, crater numbers were rescaled by the area-time function (ATF) defined in Daubar et al. (2013) to give the production function in units of impacts/km^2/yr (ATF=143 499 219 km^{2}yr for Malin et al. (2006), ATF = 19 718 204 km^{2}yr for Daubar et al. (2013)). Third, to determine cratering rates for larger diameter craters, whose formation has so far not been observed, the Hartmann (2005) 1 Gyr isochron was extrapolated to a 1 yr isochron by multiplying the incremental crater numbers by 10^{-9}, followed by a further rescaling by 1/3 in order to match the observational data. This rescaling is the same as used by Teanby and Wookey (2011), which only used the Malin et al. (2006) observations.

Because of the uncertainty surrounding the diameter threshold for atmospheric suppression of small crater diameters, I consider two impact models for the present-day crater production function:

Impact model 1: This model represents a lower bound on the present-day crater production function by assuming that the Daubar et al. (2013) observations represent the full extent of the cratering process. For craters falling in the 13.08 m diameter bin or above, the cratering rate is assumed to be given by the rescaled Hartmann (2005) 1 yr isochron. In addition to allowing extrapolation to larger crater diameters, using the rescaled isochron reduces scatter caused by small crater counts in the larger diameter bins. Error-bars are assumed to be the standard factor of 2 error discussed in Hartmann (1999, 2005). For craters in the 9.29 m bin and below the Daubar et al. (2013) results have sufficient counting statistics to be used directly. Error-bars are calculated from the Poisson statistics of the counts. This

model assumes that all the downturn at small crater diameters is caused by atmospheric ablation at a level consistent with the predictions by Popova et al. (2003) and has been fully resolved by the Daubar et al. (2013) new crater detections.

Impact model 2: This model represents an attempted best guess at the present-day crater production function, by assuming that atmospheric ablation effects are consistent with the most recent Williams et al. (2014) modelling. For craters falling in the 18.57 m diameter bin or above, the cratering rate is assumed to be given by the Hartmann (2005) isochron after rescaling to fit the Daubar et al. (2013) observations. For craters in the 13.08 m bin and below, the cratering rate is assumed to be given by the Monte Carlo model ablation/deceleration/fragmentation results presented in Williams et al. (2014) (their Figure 7a), after rescaling to fit the Daubar et al. (2013) cratering rate observed in the 9.29 and 13.08 m bins. Error-bars for the entire curve are assumed to be given by the standard factor of 2 error discussed in Hartmann (1999, 2005).

The resulting composite crater production functions are shown in Figure 1 and specified in Table 1. Certain caveats apply to these impact models: (1) using the observational studies implies that all new craters in the regions studied were identified; (2) the production functions may have varied in the past (Quantin et al., 2007; JeongAhn and Malhotra, 2014), so are only applicable to the present day; and (3) the impact rate may be dependent on Mars' orbital phase as the high orbital eccentricity takes Mars closer or further from the asteroid belt depending on the season (Daubar et al., 2012). Caveat (1) is the most important for this study, whereas (2) operates on

multi-millennial timescales, far beyond the scope of a space mission, and (3) may result in changes that are not resolvable over the course of the mission if impact detection rates are low. Note that for craters diameters $\gtrsim$10 m both impact models are lower by 1/3 than Hartmann (2005)'s isochrons, although they are just about consistent with the uncertainties he originally proposed. The difference could be due to uncertainties in the relative impactor source population on Mars compared to the Moon, or due to some new craters escaping detection with CTX. However, for the purposes of determining seismic detection rates, the impact models presented here provide a reasonable and somewhat conservative estimate of current cratering rates.

3. Estimation of Seismogram Amplitude

When studying seismograms, we are primarily interested in detecting the first arrival as this is often the most distinct. SEIS-SP is a velocity sensor and measures the ground velocity caused by seismic waves. To estimate the peak ground velocity of the first arrival for a particular impact I use analogue data from terrestrial impacts, lunar impacts, and terrestrial explosions to determine an empirical relation between impact energy, source-receiver distance, and maximum seismogram amplitude. A range of continental settings are considered in order to obtain sufficient statistics and uncertainty estimates. The variability in these data are representative of variability in Earth's crustal properties and source coupling and so also provides a measure of potential variability on Mars. Where possible I used broadband or extended short-period recordings with sample rates of 100Hz to be most directly comparable with the SEIS-SP instrument and to ensure that high

seismic frequencies were captured. The impact dataset is relatively small and comprises the Bolivian Carancas event, artificial lunar impacts, and missile impact tests. These data are supplemented with chemical and nuclear explosion data, which are often considered as a close analogue to impact sources (Teanby and Wookey, 2011). Source-receiver offsets up to 1200km are considered, i.e. regional data dominated by crustal and upper mantle structure that will be largely insensitive to differences in deep internal structure (Kennett, 2003).

3.1. Impact Data

3.1.1. Lunar Apollo Artificial Impacts

The Apollo seismic experiment is summarised in Latham et al. (1969, 1970a) and Nakamura et al. (1982) and included both long- and short-period seismometers deployed by the astronauts. Many natural and artificial impacts were detected with the Apollo seismometers (Oberst and Nakamura, 1987; Gudkova et al., 2011). Here I only consider artificial impacts by the spent Saturn V Apollo booster stage (SIVB) and the ascent stage of the lunar module (LM) as they have known impact velocities, masses, locations, and times, so provide a set of controlled sources with known properties (Table 2).

For closest comparison with SEIS-SP, I consider the Apollo short-period seismometer data, which was operated with a sample rate of around 48 Hz. Many of these recordings had low signal-to-noise, which make identification of the first arrivals and amplitudes difficult. Therefore, I selected the three impacts with the largest signal-to-noise, which were the Apollo 14 LM, the Apollo 16 SIVB, and the Apollo 17 SIVB. The locations of these impacts in relation to the Apollo seismometers are shown in Figure 2a. Seismic data

from the impacts recorded on the Apollo 14, 15, and 16 seismometers are shown in Figure 3.

3.1.2. Bolivian Carancas Impact Crater

The Carancas impact event occurred on 15$^{\text{th}}$ September 2007 at 16:40:14 UT and produced a 13.5 m diameter crater (Brown et al., 2008; Le Pichon et al., 2008; Tancredi et al., 2009). Estimates of source properties are summarised in Table 2. Seismic waves generated by the impact were recorded on the Bolivian Seismic Network (BSN) of 1 Hz short-period sensors at 50 Hz sample rate and on the Global Seismic Network (GSN) LPAZ station broadband and short-period sensors at 40 Hz sample rate. I consider the LPAZ data as slightly more reliable than the BSN data, as the sensor specification is higher. Also, absolute amplitudes can be more reliably recovered from LPAZ as full instrument transfer functions were available, whereas only approximate sensor gains were available for the BSN stations. The location of the impact is shown in Figure 2b and seismic data for the impact are shown in Figure 4. The Carancas impact event is the only example of direct seismic waves from an impact event on Earth. Other events have only been recorded seismically via ground coupling of an associated airburst. It is important to note that the impact occurred in water saturated soil and may have produced a larger crater than would have been created in solid rock. Tancredi et al. (2009) estimate that an impact energy of 1000–3000 kg TNT would be required to form the crater in this terrain. Soil water saturation could also effect the efficiency of seismic wave generation and is a sub-optimal analogue for the surface of Mars.

3.1.3. Nevada Missile Tests

In preparation for the Apollo seismic experiment Latham et al. (1970b) investigated seismic signals generated by five missile impacts at White Sands Nevada test site during 1968 and 1969. Seismograms were recorded with small geophones on analogue equipment and were used to determine the maximum ground displacements for P-waves and Rayleigh waves (Latham et al., 1970b, their Table 2). P-wave displacements were converted into maximum velocity amplitudes using a harmonic wave approximation and the reported dominant frequencies. Unfortunately the raw seismic data and instrument specifications are not available, so this approximation will introduce some uncertainty.

3.2. Explosion Data

3.2.1. EAGLE Chemical Explosions

The Ethiopia-Afar Geoscientific Lithospheric Experiment (EAGLE) is a large international project to study the Ethiopian segment of the east African rift (Maguire et al., 2003). Part of the project involved a controlled source phase in January 2003, where 23 explosive sources with yields from 50–5750 kg TNT were used to image the rift (Maguire et al., 2006). I used the 11 shot points with the highest signal-to-noise, which are summarised in Table 2. Explosions were recorded on a dense network of ≈1000 geophones and 93 broadband sensors covering an area approximately 300 x 300 km shown in Figure 2c. Here, I only consider the broadband data, which were recorded at 100 Hz on Guralp 6TD sensors. The combination of dense coverage with broadband instruments and a large number of explosive sources means this dataset is extremely well suited to studying regional amplitude

dependence.

3.2.2. Nuclear Explosions

To extend the EAGLE chemical explosion dataset to larger yields and greater source-receiver distances I also consider seismic data from nuclear tests in the US, China, and North Korea (Democratic People's Republic of Korea, DPRK). The analysis is restricted to tests conducted after 1990, where high quality seismic data are available, and to tests with reliable source yield estimates. Source parameters for these tests are given in Table 2 and locations are shown in Figure 2d–f.

3.3. Data Extraction and Processing

All data were extracted from the Incorporated Research Institutions for Seismology (IRIS) database in full Standard for the Exchange of Earthquake Data (SEED) format, except for Bolivian Seismic Network data, which were obtained directly from the Observatorio San Calixto, Bolivia (E. Minaya *pers. comm.*) in Group of Scientific Experts (GSE) format. For ease of manipulation, SEED data were converted into Seismic Analysis Code (SAC) format (Goldstein et al., 2003; Helffrich et al., 2013) using the `rdseed` utility from IRIS. An initial visual quality control step was performed using SAC to remove very noisy, clipped, or otherwise corrupted data. Instrument responses were deconvolved using the response (RESP) files supplied with SEED volumes, during which a frequency taper was applied to limit deconvolution to frequencies within the instruments' response range and prevent deconvolution instabilities. The exception to this was the BSN data, which were simply rescaled with the supplied linear sensor gains. Deconvolution converted raw

sensor counts and voltages into physical velocity units (ms^{-1}). Below 1 Hz recordings were generally contaminated by microseismic noise. Therefore, a 1–16 Hz 4 pole Butterworth filter (Gubbins, 2004) was applied to remove microseismic noise, long-period instrument drift, and high frequency noise, which helped identification of the first arrivals. The peak seismogram amplitude, i.e. the maximum ground velocity of the first arrival, was obtained from the various datasets as follows.

First, data were formed into common shot gathers and sorted in order of source-receiver distance to form record section plots as in Figure 5. This allowed identification of different arrival phases by comparison with standard travel time curves. Here I focus on the first arrivals, which on regional scales are crustal and mantle phases such as Pg and Pn (Kennett, 2003).

Second, a first arrival time window and a preceding noise time window were defined in order to estimate the maximum amplitude and associated uncertainty. Datasets were small enough that first arrival and noise windows could be picked by hand for all datasets except EAGLE, where there were over a thousand seismograms. For the EAGLE data, I used a window ± 5 s relative to the shot origin time in terms of reduced time (Shearer, 2009) assuming a p-wave velocity of 6km/s (following Maguire et al., 2006). The noise window was defined as 5–20 s before the reduced origin time. This was manually checked for each shot's record section to make sure that the first arrivals were included in the time window. The emergent lunar seismograms did not have a distinct first arrival phase so a first arrival window length of 20 s was chosen.

Third, the peak signal amplitude in the first arrival window was extracted,

along with the peak noise amplitude in the noise window, which was used to assign an uncertainty to each peak amplitude. Note that for the lunar seismograms the choice of a 20 s first arrival window length has an effect on the peak signal amplitude, with longer windows resulting in higher peak signal (reasonable choices give consistent results to within a factor of two). Amplitudes with a signal-to-noise ratio less than five were rejected from further analysis. I also examined the maximum of the envelope function obtained from the Hilbert transform of the seismogram (Shearer, 2009). However no significant difference between peak amplitudes and envelope function maxima were observed in the filtered seismograms, so I used peak amplitude for simplicity.

Therefore, for each individual seismogram, the above procedure resulted in a source yield, a source-receiver distance, a first arrival peak ground velocity, and an associated uncertainty. The results from the continental settings used in this study should be broadly transferable to Mars (see Section 5). However, care must be taken in the case of the EAGLE study, where active rifting is occurring. Maguire et al. (2006) found normal crystalline crust away from the rift's central axis, but report strong reverberations due to possible intrusions in the rift centre, which caused anomalously high amplitudes at 80–180 km offsets. These offsets were rejected from further analysis.

3.4. Distance-Yield-Amplitude Relation

Analysis of the seismic data resulted in a set of impact or explosion yields y_0 (kg TNT equivalent), source-receiver distances x_0 (km), maximum ground velocities v (ms^{-1}), and uncertainties σ_v (ms^{-1}). Inspection of this data

suggested a power law dependence of the form:

$$v(x_0, y_0) \quad = \quad a_0 x_0^b y_0^c \tag{2}$$

where a_0, b, and c are empirically derived constants. The physical meaning of these parameters is as follows. Parameter a_0 is directly proportional to the seismic efficiency k_s, which is the fraction of the impact or explosion energy converted into seismic energy. Parameter b should have a value of approximately -1 for spherically propagating waves in an isotropic medium with no attenuation. However, attenuation will reduce the value of b and non-spherical propagation due to crustal velocity gradients will also affect b. Parameter c, the dependence on yield, has been much debated in the literature, with values in the range 1/3–1 being suggested (see discussion in Kohler and Fuis, 1992). The most comprehensive study is that of Larson (1982), who found a value of around 1/3 using yields spanning 10 orders of magnitude in sodium chloride (laboratory scales to large nuclear tests). If only energy conservation is considered, a value of $c = 1/2$ would be expected, as the kinetic energy of an elastic seismic wave is proportional to the ground velocity squared.

The parameters a_0, b, and c were fitted to the explosive dataset using unweighted linear least squares (Gubbins, 2004). The fitted value of c was 0.49 ± 0.03, which is indistinguishable from the idealised energy conservation value of 1/2. Therefore, c was fixed at 1/2 and the other parameters were refitted to simplify subsequent analysis. The fit parameters and uncertainties are given in Table 3. Figure 6 shows the fitted relationship for $v(x_0, y_0)$, where the velocity has been rescaled to that of a standard 1000 kg TNT

source using:

$$v(x_0, 1000 \text{ kg TNT}) \;=\; v(x_0, y_0) \left(\frac{1000 \text{ kg TNT}}{y_0} \right)^{1/2} \qquad (3)$$

The relationship is linear (in logarithmic space) over a wide range of source-receiver distances and explosive yields. Unfortunately, there are not enough impact data to reliably fit the parameters a_0, b, and c to impacts alone. Therefore, my approach is to use the explosive data as a basis for extrapolation to the impact case.

Further consideration is required before translating the fitted parameters from explosive sources to impacts sources. As shown in Figure 6, explosions generally give higher peak velocities than impacts. This is primarily because explosives are buried to maximise the seismic coupling in controlled source experiments like EAGLE; or in the case of nuclear weapons testing, to avoid surface damage and undesirable radioactive fallout. Therefore, explosives tend to have a higher seismic efficiency and a correspondingly higher value for the a_0 parameter (see also discussion of seismic efficiency in Richardson et al., 2005; Teanby and Wookey, 2011). However, the effect of distance is entirely dependent on crustal properties and wave propagation, so parameter b can be assumed to be the same for both impacts and explosions. Note that the Moon is known to have a high seismic Q (low seismic attenuation) (Nakamura and Koyama, 1982; Lognonne and Mosser, 1993; Lognonne et al., 2003) and emergent arrivals due to crustal scattering. Inspection of Figure 6 shows that the lunar impacts have the same source-receiver distance dependence as terrestrial explosions, so the high Q does not significantly affect the distance dependence of peak seismogram amplitudes on regional scales. However, this could be a coincidence due to competing effects of high lunar Q and high

crustal scattering. Parameter c should also have a similar value for impacts and explosions due to the similarities between these two source types; both sources are isotropic, effectively occur at a point source, and preferentially generate P-waves.

Therefore, to first order the relationship for $v(x_0, y_0)$ can be translated from explosions to impacts via application of a simple scale factor s to the a_0 parameter. To allow constraints determined from the larger explosion dataset to be used b and c were fixed and the scale factor s was fitted to the impact dataset. The best fitting value of s is 0.099, implying that buried explosions are $\sim$10 times more effective at generating seismic waves than impacts. The value of s contains an order of magnitude uncertainty due to the sparse and varied nature of the impact data. This large uncertainty is inevitable as s depends linearly on the impact seismic efficiency. The uncertainty in s places the upper error bound in line with the Apollo impact results and the lower bound in line with the LPAZ Carancas measurements. Parameters and uncertainties for the $v(x_0, y_0)$ relation for impacts are given in Table 3. Note that this relationship is only valid for events with source-receiver distances of $<$1200 km. Also, as the raw data is bandpass filtered between 1–16 Hz, this relationship is only applicable for frequencies within the 1–16 Hz range.

4. Regional Impact Detection

Consider an impact with yield y_0 (kg TNT equivalent) a distance x_0 (km) from the SEIS-SP seismometer. From Section 3 the peak ground velocity $v(x_0, y_0)$ (ms^{-1}) of the first arrival from is:

$$v(x_0, y_0) \quad = \quad a_0 s x_0^b y_0^c \tag{4}$$

The yield of TNT is q=4.18×10^6 J/kg (Shoemaker, 1983), so in SI units equation 4 becomes:

$$v(x,y) = a_0 s \left(\frac{1}{1000}\right)^b \left(\frac{1}{q}\right)^c x^b y^c \quad (5)$$

$$(6)$$

where x has units of meters and y has units of Joules. This can be simplified by setting:

$$a = a_0 s \left(\frac{1}{1000}\right)^b \left(\frac{1}{q}\right)^c \quad (7)$$

which gives:

$$v(x,y) = a x^b y^c \quad (8)$$

Constraints on the impact rate from section 2 are in terms of crater diameter D (meters), which is related to impact energy y (Joules) by (Teanby and Wookey, 2011):

$$D = \alpha_\oplus y^\beta \left(\frac{g_\oplus}{g}\right)^{3/16} \quad (9)$$

where $\alpha_\oplus$ and β are empirically derived constants, $g_\oplus$ is Earth's gravity, and g is the gravity on Mars. Setting:

$$\alpha = \alpha_\oplus \left(\frac{g_\oplus}{g}\right)^{3/16} \quad (10)$$

Gives $D = \alpha y^\beta$ and:

$$y = \left(\frac{D}{\alpha}\right)^{1/\beta} \quad (11)$$

So, in terms of crater diameter, the peak ground velocity on Mars is:

$$v(x, D) = ax^b \left(\frac{D}{\alpha}\right)^{c/\beta} \quad (12)$$

As is conventional for broadband seismometers, the noise level of SEIS-SP is specified in terms of acceleration noise power spectral density p_a ($\mathrm{ms}^{-2}\mathrm{Hz}^{-1/2}$). The corresponding velocity noise power spectral density p_v ($\mathrm{ms}^{-1}\mathrm{Hz}^{-1/2}$) at frequency f is:

$$p_v = \frac{p_a}{2\pi f} \quad (13)$$

The peak velocity noise n_v (in ms^{-1}) in the frequency range f_1–f_2 is given by (Havskov and Alguacil, 2004):

$$n_v = \frac{5}{4} p_v \sqrt{f_2 - f_1} \quad (14)$$

Combining equations 13 and 14 with the geometric mean central frequency $f = \sqrt{f_1 f_2}$ gives:

$$n_v = \frac{5}{8\pi} p_a \sqrt{\frac{1}{f_1} - \frac{1}{f_2}} \quad (15)$$

For an event to be detectable the signal must be greater than the noise. Therefore, the maximum source-receiver distance x_{max} where an impact is detectable is given by the criteria:

$$v(x_{max}, D) = n_v \quad (16)$$

Combining equations 12, 15 and 16 gives the detection criteria:

$$a x_{max}^b \left(\frac{D}{\alpha}\right)^{c/\beta} = \frac{5}{8\pi} p_a \sqrt{\frac{1}{f_1} - \frac{1}{f_2}} \quad (17)$$

Therefore,

$$x_{max}(D) = \left(\frac{5}{8\pi}p_a\sqrt{\frac{1}{f_1}-\frac{1}{f_2}}\right)^{1/b}\alpha^{c/b\beta}a^{-1/b}D^{-c/b\beta} \quad (18)$$

Equation 18 gives the criteria for the maximum detection range $x_{max}(D)$ of an impact crater with diameter D for an instrument with an acceleration noise power spectral density of p_a in the frequency range f_1 – f_2. If the source-receiver distance x is less than x_{max} then the impact will be detectable, otherwise it will be below the instrument noise. The values of the parameters and their fractional errors are given in Table 3. Note that parameters a, b, and c are potentially frequency dependent and application of equation 18 outside the 1–16 Hz frequency range would require these parameters to be redetermined.

To determine the impact detection rate with SEIS-SP the crater production functions from section 2 must be combined with the detection criteria in equation 18. First, equation 18 is used to determine the maximum detection range of a crater with a given diameter. I use the SEIS-SP instrument specification of p_a=10^{-8} $ms^{-2}Hz^{-1/2}$ (Lognonne et al., 2014) and a frequency range of 1–16 Hz, which corresponds to that used to determine the parameter values and is appropriate for regional events. Fractional parameter errors are propagated through equation 18 using the formulae in Bevington and Robinson (1992) (Figure 7a). The detection range predictions are reliable up to source-receiver distances of 1200 km, beyond which the regional phases used to determine the amplitude dependence may no longer be appropriate. Therefore, x_{max} is limited to a maximum value of 1200 km. Second, the detection range is converted into the fractional area of Mars f_a using

geometry:

$$f_a(D) = \frac{1}{2}\left[1 - \cos\left(\frac{x_{max}(D)}{r_{mars}}\right)\right] \quad (19)$$

where r_{mars} is the radius of Mars (Figure 7b). Finally the detectable fraction is multiplied by the crater production functions (Figure 7c) to give the detection rate $N_{det}(D)$ for each crater diameter bin:

$$N_{det}(D) = f_a(D)N(D) \quad (20)$$

The resulting detection rates are plotted in Figure 7d for the two impact models. The total number of regional impacts detected is given by the sum of $N_{det}(D)$ over all crater diameters. For impact model 1 there is nominally 1 detectable impact per year with a 1-σ range of 0.1-10 year^{-1}, whereas for impact model 2 there are nominally 3 detectable impacts per year with a 1-σ range of 0.3-30 year^{-1}. The most commonly detected impacts are expected to have crater diameters of 5–20 m (impact model 1) and 0.5–20 m (impact model 2).

5. Discussion

Overall, I predict around 1–3 regional impacts per year will be detectable by SEIS-SP with a 1-σ uncertainty range of 0.1–30 year^{-1}.

The primary source of the order of magnitude uncertainty is scatter in the measured impact generated peak seismogram amplitudes, which originates from variations in crustal properties, data quality, and seismic efficiency. The scatter in both impact and explosion datasets illustrates the high variability possible in seismic coupling, even within similar terrains such as for the EAGLE experiment. A fundamental limitation is the uncertainty and variability

in seismic efficiency, which depends on individual site and impact conditions. It is reasonable to expect similar variations and subsequent uncertainties on Mars. A secondary source of uncertainty is the size frequency distribution of impact crater generation, which depends critically on the diameter where atmospheric ablation, deceleration, and fragmentation become important. However, this effect is not as important as might be expected; the two end member impact models only change the number of detectable events by a factor of $\sim$3. This is because smaller craters, which are the most heavily affected by the atmosphere, are only detectable over a very limited range.

If we are optimistic and regard the low amplitudes from the Carancas event as anomalous and the Apollo and White Sands missile impact results as more representative of Mars' expected seismogram amplitudes, then around 10–30 regionally detectable events per year are predicted. This is tempting as the Apollo / White Sands results define a consistent trend with a similar distance dependence to the larger and more reliable terrestrial explosion dataset. However, given the sparse nature of the impact dataset, rejecting any of the datapoints is not advisable.

The analysis presented here assumes the impact and explosion data used to develop the distance-yield-amplitude scaling relation are a reasonable analogue for determining seismic amplitudes on Mars. The validity of this approach depends on the attenuation and scattering properties of Mars' crust and upper mantle, and how these compare to the Earth and Moon. For example, the lunar regolith is highly fractured and gardened, with very high scattering. It is also very dry with very low seismic attenuation (high Q). While Mars' bulk attenuation has been determined from the secular acceler-

ation of Phobos (Smith and Born, 1976; Zharkov and Gudkova, 1997), it is not possible to uniquely extract crustal and upper mantle Q values.

Lognonne and Mosser (1993) discuss the potential attenuation of Mars' crust and mantle and conclude that martian mantle has a Q value between Earth's upper and lower mantle. Lognonne and Mosser (1993) also argue that Mars' crust should be less attenuating than Earth's because of enhanced removal of trapped fluids from crustal rocks due to Mars' low atmospheric surface pressure. However, Mars' crust should be more attenuating than the Moon, where exposure to a hard vacuum will have removed the majority of trapped fluids leading to very low attenuation (high Q).

Crustal scattering on Mars should be present at greater levels than on Earth because of the influence of the large number of impact craters, which fracture and brecciate the upper crustal layers (Lognonne and Mosser, 1993). However, Mars' increased gravity and more geologically active surface should mean that scattering is far less important than on the Moon. In summary, we might expect attenuation and scattering for Mars to lie somewhere between Earth and Moon end members. Therefore, as the fitted distance-yield-amplitude scaling law spans lunar and terrestrial impacts, it should provide a reasonable approximation to the seismic behaviour of Mars' crust and upper mantle.

Despite the large uncertainties, it is interesting to compare the regional predictions to global modelling results from Teanby and Wookey (2011), who considered the frequency range 0.4–4 Hz. For a nominal SEIS-VBB noise level of 10^{-9} $ms^{-2}Hz^{-1/2}$, Teanby and Wookey (2011) predicted that ≈1 event per year would be detectable at 1000 km range or more, and that ≈0.1 events

per year would detectable globally, with an order of magnitude uncertainty. For a noise level of 10^{-8} $ms^{-2}Hz^{-1/2}$, which is relevant for the SEIS-SP, these estimates became ≈0.1 and ≈0.01 events per year respectively - i.e. at the lower end of the present study's uncertainty range. The results presented here are appropriate for regional source-receiver distances of ≈1200 km or less, whereas the modelling results of Teanby and Wookey (2011) are valid for teleseismic source-receiver distances over 1000 km, which means the scaling relation results must be extrapolated somewhat to effectively compare the studies. This extrapolation is indicated by the grey lines in Figure 7. Figure 7d shows that both sets of results are only just consistent to within the errors of each study. However, much better agreement is obtained if the modelling in Teanby and Wookey (2011) is repeated using a seismic efficiency of k_s=5×10^{-4} instead of k_s=2×10^{-5} that was used in the original study (Figure 7d). A value of k_s=5×10^{-4} is roughly consistent with the upper end of laboratory studies and modelling (Güldemeister et al., 2013; Richardson and Kedar, 2013; Richardson et al., 2005; Schultz and Gault, 1975) and thus may be more appropriate for impact processes.

It is possible that the actual noise spectral density of SEIS-SP could be somewhat different to that specified in the mission requirements. Therefore, I have repeated the analysis in Section 4 with a range of noise levels from 10^{-9}–10^{-7} $ms^{-2}Hz^{-1/2}$. The number of detections in each case are summarised in Table 4, including the extrapolation for impacts beyond 1200 km. Note that for instrument noise spectral densities below ∼10^{-9} $ms^{-2}Hz^{-1/2}$ the ambient noise is likely to be the dominant noise source. Noise on Mars is primarily determined by the wind and is expected to vary between 10^{-10}–

10^{-8} $ms^{-2}Hz^{-1/2}$ (Lognonne and Mosser, 1993), depending on the time of day and season.

Atmospheric fragmentation of meteoroids before impact could also affect detection rates. Both Malin et al. (2006) and Daubar et al. (2013) observed clusters of craters at the new impact sites indicating that fragmentation had occurred. In the Daubar et al. (2013) study this occurred at 56% of sites. A cluster of impacts will give a more complex and lower amplitude seismic signal than a single large impact (Banks et al., 2015). To investigate the effects of this I consider a worst case scenario where the amplitude of the seismic signal generated would be determined by the largest fragment only. Williams et al. (2014) modelled the fragmentation process, which included a meteoroid strength parameter that was adjusted to match fragmentation rates observed by Daubar et al. (2013). I consider Williams et al. (2014)'s high fragmentation case and use this to determine the size-frequency distribution (SFD) of individual craters from Daubar et al. (2013)'s reported effective diameters for the new impact sites. First, I convert the incremental Daubar et al. (2013) SFD into a cumulative SFD to remove the dependence on bin width. Second, I correct for underestimation bias in D_{eff} caused by deceleration and ablation using the relation in Williams et al. (2014) (their Figure 8b). Third, the corrected SFD is modified using the ratio of fragmentation to no-fragmentation crater production from Williams et al. (2014) (their Figure 7b). Finally, the cumulative SFD is converted back into an incremental SFD. Figure 8 compares the SFD of effective crater diameters from Daubar et al. (2013) with the corresponding distribution of individual craters assuming the fragmentation model of Williams et al. (2014). For

craters in the 2–40 m diameter range, fragmentation reduces the number of individual craters by a factor of 0.7 compared to the SFD of effective crater diameters. Therefore, while the effect of fragmentation is important, it is relatively small compared to the order of magnitude uncertainties introduced by the distance-yield-amplitude scaling relation.

Finally, the results presented here relate to the detectability of first arrival Pn and Pg phases. These are high frequency phases suitable for detection with SEIS-SP in the 1–16 Hz bandwidth. However, both SEIS-SP and SEIS-VBB have sensitivity at lower frequencies (<1 Hz) where other later arriving phases may be observed. In particular, the SEIS-VBB will be able to detect long-period surface waves, which often have higher amplitudes than the first arrivals (e.g. Benz et al., 1997; Chun and Henderson, 2009). This suggests that if the Pn or Pg phase is detectable then the surface waves should also be observed. Conversely, there should also be some events for which only the surface waves are detectable, although these will be much more challenging to interpret.

6. Conclusions

In this study I estimate the number of meteorite impacts detectable on Mars with the InSight SEIS-SP instrument to be 0.1–30 year^{-1} with a nominal detection rate of 1–3 year^{-1}. These detection rates are appropriate for Pn and Pg phases on regional scales and assume a nominal instrument noise of 10^{-8} ms^{-2}Hz$^{-1/2}$ and a frequency bandpass of 1–16 Hz. Seismic data from impacts and explosions were used to determine an empirical scaling relation between peak ground velocity, source-receiver distance, and impact yield.

Comparison of explosion and impact datasets showed that buried explosives are ∼10 times more efficient at generating seismic waves than surface impacts. The available impact dataset is quite limited and scatter in the measured amplitudes caused by variations in seismic efficiency and crustal properties is the major source of uncertainty in this study. A secondary source of uncertainty is knowledge of the current crater production function on Mars. Two impact models were tested, compiled from observational sources (Malin et al., 2006; Daubar et al., 2013), modelling (Williams et al., 2014), and standard isochrons (Hartmann, 2005). Choice of impact model changed the predictions by a factor of ∼3. An additional minor source of error was the effect of atmospheric fragmentation.

Comparison with the modelling study of Teanby and Wookey (2011) is possible for intermediate sized craters with 20–80 m diameters at source-receiver distances of around 1000–3000 km, which suggests that a seismic efficiency of $\sim 5 \times 10^{-4}$ may be appropriate for impact processes. This is consistent with laboratory and modelling results and is more optimistic than the value of 2×10^{-5} originally used by Teanby and Wookey (2011). If $k_s = 5 \times 10^{-4}$ is appropriate then the estimates of Teanby and Wookey (2011) can be revised upwards from ≈0.1 to ≈1 globally detectable impact events per year assuming a noise of 10^{-9} ms^{-2}Hz$^{-1/2}$ for the SEIS-VBB. However, seismic efficiency remains a major source of uncertainty in this work and further laboratory and field investigation is required.

For the nominal detection rate (1–3 year^{-1}) or at the more optimistic end of the uncertainties (10–30 year^{-1}), regional impacts should provide a viable way to study the crust and upper mantle of Mars, especially if the new

impact craters are locatable from orbit. Seismic recordings of impact events will be complementary to any fault generated seismicity, providing different frequency content, more uniform spatial distribution, and the potential for accurately located events using orbital imagery. A single located impact could begin to constrain crust and upper mantle velocities and the seismic efficiency of the cratering process. For 5–10 impacts detected at a range of distances, crude record sections could be constructed and used to identify more complex seismic phases. Such a dataset could also be used to more fully constrain seismic efficiency and study current cratering rates on Mars.

7. Acknowledgements

This work was funded by the UK Science and Technology Facilities Council and the UK Space Agency. The author would like to thank Estela Minaya (Observatorio San Calixto, Boliva) and David Green (AWE Blacknest) for assistance with the BSN data, Peter Maguire for providing information on the EAGLE shot points, and James Wookey for insightful discussions. Mark Panning and Ingrid Daubar provided helpful and constructive reviews that improved the manuscript significantly.

References

Acuna, M.H., Connerney, J.E.P., Ness, N.F., Lin, R.P., Mitchell, D., Carlson, C.W., McFadden, J., Anderson, K.A., Reme, H., Mazelle, C., Vignes, D., Wasilewski, P., Cloutier, P., 1999. Global distribution of crustal magnetization discovered by the Mars Global Surveyor MAG/ER experiment. Science 284, 790–793.

735 Anderson, D.L., Duennebier, F.K., Latham, G.V., Toksoz, M.F., Kovach,
736 R.L., Knight, T.C.D., Lazarewicz, A.R., Miller, W.F., Nakamura, Y., Sut-
737 ton, G., 1976. Viking seismic experiment. Science 194, 1318–1321.

738 Banks, M.E., Daubar, I.J., Schmerr, N.C., Golombek, M.P., 2015. Predicted
739 seismic signatures of recent dated martian impact events: implications for
740 the InSight lander, in: Lunar and Planetary Science Conference, p. 2679.

741 Benz, H.M., Frankel, A., Boore, D.M., 1997. Regional Lg attenuation for the
742 continental United States. Bull. Seism. Soc. Am. 87, 606–619.

743 Bevington, P.R., Robinson, D.K., 1992. Data reduction and error analysis
744 for the physical sciences. WBC/McGraw-Hill, New York. 2nd edition.

745 Brown, P., ReVelle, D.O., Silber, E.A., Edwards, W.N., Arrowsmith, S.,
746 Jackson, L.E., Tancredi, G., Eaton, D., 2008. Analysis of a crater-forming
747 meteorite impact in Peru. J. Geophys. Res. 113, E09007.

748 Chun, K.Y., Henderson, G.A., 2009. Lg attenuation near the North Korean
749 border with China, part II: Model development from the 2006 nuclear
750 explosion in North Korea. Bull. Seism. Soc. Am. 99, 3030–3038.

751 Connerney, J.E.P., Acuna, M.H., Wasilewski, P.J., Ness, N.F., Reme, H.,
752 Mazelle, C., Vignes, D., Lin, R.P., Mitchell, D.L., Cloutier, P.A., 1999.
753 Magnetic lineations in the ancient crust of Mars. Science 284, 794–798.

754 CTBTO, 2012. Comprehensive Test Ban Treaty Organisa-
755 tion: list of significant nuclear explosions. (available online at
756 http://www.ctbto.org/nuclear-testing/types-of-nuclear-weapons)
757 .

758 Dandonneau, P.A., Lognonne, P., Banerdt, W.B., Deraucourt, S., Gabsi,
759 T., Gagnepain-Beyneix, J., Nebut, T., Robert, O., Tillier, S., Hurst, K.,
760 Mimoun, D., Christenssen, U., Bierwirth, M., Roll, R., Pike, T., Calcutt,
761 S., Giardini, D., Mance, D., Zweifel, P., Laudet, P., Kerjean, L., Perez,
762 R., Seis Team, 2013. The SEIS InSight VBB Experiment, in: Lunar and
763 Planetary Science Conference, p. 2006.

764 Daubar, I.J., Golombek, M.P., McEwen, A.S., Byrne, S., Kreslavsky, M.,
765 Schmerr, N.C., Banks, M.E., Lognonné, P., Kawamura, T., Karakostas,
766 F., 2015. Measurement of the current martian cratering size frequency
767 distribution, predictions for and expected improvements from InSight, in:
768 Lunar and Planetary Science Conference, p. 2468.

769 Daubar, I.J., McEwen, A.S., Byrne, S., Kennedy, M.R., 2012. Seasonal
770 variation in current martian impact rate, in: Lunar and Planetary Science
771 Conference, p. 2740.

772 Daubar, I.J., McEwen, A.S., Byrne, S., Kennedy, M.R., Ivanov, B., 2013.
773 The current martian cratering rate. Icarus 225, 506–516.

774 Davis, P.M., 1993. Meteoroid impacts as seismic sources on Mars. Icarus
775 105, 469–478.

776 Delahunty, A..K.., Pike, W..T.., 2014. Metal-armouring for shock protection
777 of MEMS. Sensors & Actuators A: Physical 215, 36–43.

778 Edwards, W.N., Eaton, D.W., Brown, P.G., 2008. Seismic observa-
779 tions of meteors: coupling theory and observations. Rev. Geophys. 46,
780 2007RG000253.

781 Goldstein, P., Dodge, D., Firpo, M., Minner, L., 2003. SAC2000: Signal pro-
782 cessing and analysis tools for seismologists and engineers, in: Lee, W.H.,
783 Kanamori, H., Jennings, P., Kisslinger, C. (Eds.), International Handbook
784 of Earthquake and Engineering Seismology Part B. Academic Press. vol-
785 ume 81B of *International Geophysics Series*, pp. 1613–1614.

786 Golombek, M.P., Banerdt, W.B., Tanaka, K.L., Tralli, D.M., 1992. A pre-
787 diction of Mars seismicity from surface faulting. Science 258, 979–981.

788 Gubbins, D., 2004. Time series analysis and inverse theory for geophysicists.
789 Cambridge Univ. Press, Cambridge UK.

790 Gudkova, T.V., Lognonné, P., Gagnepain-Beyneix, J., 2011. Large impacts
791 detected by the Apollo seismometers: Impactor mass and source cutoff
792 frequency estimations. Icarus 211, 1049–1065.

793 Güldemeister, N., Moser, D., Wünnemann, K., Hoerth, T., Schäfer, F., 2013.
794 Recording and investigation of the seismic signal generated by hypervelo-
795 city impact experiments and numerical models. European Planetary Science
796 Congress, 8-13 September, London 8, 550.

797 Hartmann, W.K., 1999. Martian cratering VI. Crater count isochrons and
798 evidence for recent volcanism from Mars Global Surveyor. Meteoritics and
799 Planetary Science 34, 167–177.

800 Hartmann, W.K., 2005. Martian cratering 8: Isochron refinement and the
801 chronology of Mars. Icarus 174, 294–320.

802 Havskov, J., Alguacil, G., 2004. Instrumentation in Earthquake Seismology.
803 Springer, Netherlands.

804 Helffrich, G., Wookey, J., Bastow, I., 2013. The Seismic Analysis Code: A
805 Primer and User's Guide. Cambridge Univ. Press, Cambridge.

806 JeongAhn, Y., Malhotra, R., 2014. The current impactor flux on Mars and
807 its seasonal variation, in: AAS/Division for Planetary Sciences Meeting
808 Abstracts, p. 203.08.

809 Kennett, B.L.N., 2003. The Seismic Wavefield - Volume 2, Interpretation
810 of Seismograms on Regional and Global Scales. Cambridge Univ. Press,
811 Cambridge.

812 Knapmeyer, M., Oberst, J., Hauber, E., Wahlisch, M., Deuchler, C., Wag-
813 ner, R., 2006. Working models for spatial distribution and level of Mars'
814 seismicity. J. Geophys. Res. 111, E11006.

815 Kohler, W.M., Fuis, G.F., 1992. Empirical dependence of seismic ground ve-
816 locity on the weight of explosives, shotpoint site conditions, and recording
817 distance for seismic-refraction data. Bull. Seism. Soc. Am. 82, 2032–2044.

818 Larson, D.B., 1982. Inelastic wave propagation in sodium chloride. Bull.
819 Seism. Soc. Am. 72, 2107–2130.

820 Latham, G., Ewing, M., Press, F., Sutton, G., 1969. Apollo passive seismic
821 experiment. Science 165, 241–250.

822 Latham, G.V., Ewing, M., Press, F., Sutton, G., Dorman, J., Nakamura, Y.,
823 Toksoz, N., Wiggins, R., Derr, J., Duennebi, F., 1970a. Passive seismic
824 experiment. Science 167, 455–457.

825 Latham, G.V., McDonald, W.G., Moore, H.J., 1970b. Missile impacts as
826 sources of seismic energy on the moon. Science 168, 242–245.

827 Le Pichon, A., Antier, K., Cansi, Y., Hernandez, B., Minaya, E., Burgoa,
828 B., Drob, D., Evers, L.G., Vaubaillon, J., 2008. Evidence for a meteoritic
829 origin of the September 15, 2007, Carancas crater. Meteoritics & Planetary
830 Science 43, 1797–1809.

831 Lognonne, P., Banerdt, W., Pike, T., Giardini, D., Christensen, U., Banfield,
832 D., Mimoun, D., Laudet, P., de Raucourt, S., Bierwirth, M., Zweifel, P.,
833 Calcutt, S., Hurst, K., Bruce, C., 2014. SEIS/InSight and Mars seismology:
834 development status and focus on the impact detection, in: EGU General
835 Assembly Conference Abstracts, p. 12183.

836 Lognonne, P., Gagnepain-Beyneix, J., Chenet, H., 2003. A new seismic model
837 of the Moon: implications for structure, thermal evolution and formation
838 of the Moon. Earth Planet. Sci. Let. 211, 27–44.

839 Lognonne, P., Giardini, D., Banerdt, B., Gagnepain-Beyneix, J., Mocquet,
840 A., Spohn, T., Karczewski, J.F., Schibler, P., Cacho, S., Pike, W.T.,
841 Cavoit, C., Desautez, A., Favede, M., Gabsi, T., Simoulin, L., Striebig,
842 N., Campillo, M., Deschamp, A., Hinderer, J., Leveque, J.J., Moatagner,
843 J.P., Rivera, L., Benz, W., Breuer, D., Defraigne, P., Dehant, V., Fu-
844 jimura, A., Mizutani, H., Oberst, J., 2000. The NetLander very broad
845 band seismometer. Plan. & Space Sci. 48, 1289–1302.

846 Lognonne, P., Mosser, B., 1993. Planetary seismology. Surveys in Geophysics
847 14, 239–302.

Lorenz, R.D., 2012. Planetary seismology - Expectations for lander and wind noise with application to Venus. Plan. & Space Sci. 62, 86–96.

Maguire, P.K.H., 2003. EAGLE Phase III: the controlled source seismic project. Fieldwork Report , 1–120.

Maguire, P.K.H., Ebinger, C.J., Stuart, G.W., Mackenzie, G.D., Whaler, K.A., Kendall, J.M., Khan, M.A., Fowler, C.M.R., Klemperer, S.L., Keller, G.R., Harder, S., Furman, T., Mickus, K., Asfaw, L., Ayele, A., Abebe, B., 2003. Geophysical project in Ethiopia studies continental breakup. EOS Trans. AGU 84, 337–343.

Maguire, P.K.H., Keller, G.R., Klemperer, S.L., Mackenzie, G.D., Keranen, K., Harder, S., O'Reilly, B., Thybo, H., Asfaw, L., Khan, M.A., Amha, M., 2006. Crustal structure of the northern Main Ethiopian Rift from the EAGLE controlled-source survey; a snapshot of incipient lithospheric break-up. Geological Society of London Special Publications 259, 269–292.

Malin, M.C., Edgett, K.S., Posiolova, L.V., McColley, S.M., Dobrea, E.Z.N., 2006. Present-day impact cratering rate and contemporary gully activity on Mars. Science 314, 1573–1577.

Nakamura, Y., Koyama, J., 1982. Seismic-Q of the Lunar upper mantle. J. Geophys. Res. B87, 4855–4861.

Nakamura, Y., Latham, G.V., Dorman, H.J., 1982. Apollo lunar seismic experiment - final summary. J. Geophys. Res. A87, 117–123.

Oberst, J., Nakamura, Y., 1987. Distinct meteoroid families identified on the Lunar seismograms. J. Geophys. Res. 92, E769–E773.

871 Panning, M.P., Beucler, É., Drilleau, M., Mocquet, A., Lognonné, P.,
872 Banerdt, W.B., 2015. Verifying single-station seismic approaches using
873 Earth-based data: Preparation for data return from the InSight mission
874 to Mars. Icarus 248, 230–242.

875 Pike, W.T., Standley, I.M., Banerdt, W.B., 2005. A high-sensitivity broad-
876 band seismic sensor for shallow seismic sounding of the Lunar regolith,
877 in: S. Mackwell & E. Stansbery (Ed.), 36th Annual Lunar and Planetary
878 Science Conference, p. 2002.

879 Popova, O., Nemtchinov, I., Hartmann, W.K., 2003. Bolides in the present
880 and past martian atmosphere and effects on cratering processes. Meteorit-
881 ics & Planet. Sci 38, 905–925.

882 Quantin, C., Mangold, N., Hartmann, W.K., Allemand, P., 2007. Possible
883 long-term decline in impact rates - 1. Martian geological data. Icarus 186,
884 1–10.

885 Richardson, J.E., Kedar, S., 2013. An experimental investigation of the
886 seismic signal produced by hypervelocity impacts, in: Lunar and Planetary
887 Science Conference, p. 2863.

888 Richardson, J.E., Melosh, H.J., Greenberg, R.J., O'Brien, D.P., 2005. The
889 global effects of impact-induced seismic activity on fractured asteroid sur-
890 face morphology. Icarus 179, 325–349.

891 Roberts, G.P., Matthews, B., Bristow, C., Guerrieri, L., Vetterlein, J., 2012.
892 Possible evidence of paleomarsquakes from fallen boulder populations, Cer-
893 berus Fossae, Mars. J. Geophys. Res. 117, E003816.

Schultz, P.H., Gault, D.E., 1975. Seismic effects from major basin formations on the Moon and Mercury. The Moon 12, 159–177.

Shearer, P.M., 2009. Introduction to Seismology. Cambridge Univ. Press, Cambridge. 2nd edition.

Shoemaker, E.M., 1983. Asteroid and comet bombardment of the earth. Annual Review of Earth and Planetary Sciences 11, 461–494.

Smith, J.C., Born, G.H., 1976. Secular acceleration of Phobos and Q of Mars. Icarus 27, 51–53.

Sohl, F., Schubert, G., Spohn, T., 2005. Geophysical constraints on the composition and structure of the Martian interior. J. Geophys. Res. 110, E12008.

Sohl, F., Spohn, T., 1997. The interior structure of Mars: Implications from SNC meteorites. J. Geophys. Res. E102, 1613–1635.

Tancredi, G., Ishitsuka, J., Schultz, P.H., Harris, R.S., Brown, P., ReVelle, D.O., Antier, K., Le Pichon, A., Rosales, D., Vidal, E., Varela, M.E., Sanchez, L., Benavente, S., Bojorquez, J., Cabezas, D., Dalmau, A., 2009. A meteorite crater on earth formed on September 15, 2007: The Carancas hypervelocity impact. Meteoritics & Planetary Science 44, 1967–1984.

Taylor, J., Teanby, N.A., Wookey, J., 2013. Estimates of seismic activity in the Cerberus Fossae region of Mars. J. Geophys. Res. E118, 2570–2581.

Teanby, N.A., Wookey, J., 2011. Seismic detection of meteorite impacts on Mars. Phys. Earth Planet. Int. 186, 70–80.

916 Toksoz, M.N., Dainty, A.M., Solomon, S.C., Anderson, K.R., 1974. Structure
917 of the Moon. Rev. Geophys. & Space Phys. 12, 539–567.

918 U. S. Department of Energy, 2000. United States nuclear
919 tests: July 1945 through September 1992. (available online at
920 http://www.nv.doe.gov/library/publications/historical/DOENV_209_REV15.pdf)
921 DOE/NV 209 Rev. 15, 1–185.

922 Williams, D.R., 2003. Impact sites of Apollo LM
923 ascent and SIVB stages. (available online at
924 http://nssdc.gsfc.nasa.gov/planetary/lunar/apollo_impact.html)
925 .

926 Williams, J.P., Pathare, A.V., Aharonson, O., 2014. The production of small
927 primary craters on Mars and the Moon. Icarus 235, 23–36.

928 Yang, X., North, R., Romney, C., Richards, P., 2003. Worldwide nuclear ex-
929 plosions, in: Lee, W.H., Kanamori, H., Jennings, P., Kisslinger, C. (Eds.),
930 International Handbook of Earthquake and Engineering Seismology Part
931 B. Academic Press. volume 81B of *International Geophysics Series*, pp.
932 1595–1599.

933 Yoder, C.F., Konopliv, A.S., Yuan, D.N., Standish, E.M., Folkner, W.M.,
934 2003. Fluid core size of Mars from detection of the solar tide. Science 300,
935 299–303.

936 Zhang, M., Wen, L., 2013. High-precision location and yield of North Korea's
937 2013 nuclear test. Geophys. Res. Lett. 40, 2941–2946.

938 Zharkov, V.N., Gudkova, T.V., 1997. On the dissipative factor of the Martian
939 interiors. Plan. & Space Sci. 45, 401–407.

940 Zharkov, V.N., Gudkova, T.V., 2005. Construction of martian interior model.
941 Solar System Research 39, 343–373.

942 Zuber, M.T., 2001. The crust and mantle of Mars. Nature 412, 220–227.

			Impact Model 1				Impact Model 2			
D	D_1	D_2	N	N_{min}	N_{max}		N	N_{min}	N_{max}	
(m)	(m)	(m)	($km^{-2}\,yr^{-1}$)	($km^{-2}\,yr^{-1}$)	($km^{-2}\,yr^{-1}$)		($km^{-2}\,yr^{-1}$)	($km^{-2}\,yr^{-1}$)	($km^{-2}\,yr^{-1}$)	
0.0514	0.0432	0.0611	-	-	-		6.41×10^{-07}	3.21×10^{-07}	1.28×10^{-06}	‡
0.0725	0.0610	0.0863	-	-	-		3.86×10^{-06}	1.93×10^{-06}	7.72×10^{-06}	‡
0.103	0.086	0.122	-	-	-		1.46×10^{-05}	7.28×10^{-06}	2.91×10^{-05}	‡
0.145	0.122	0.173	-	-	-		4.71×10^{-05}	2.36×10^{-05}	9.43×10^{-05}	‡
0.206	0.173	0.245	-	-	-		1.02×10^{-04}	5.09×10^{-05}	2.04×10^{-04}	‡
0.290	0.244	0.345	-	-	-		1.25×10^{-04}	6.23×10^{-05}	2.49×10^{-04}	‡
0.411	0.345	0.488	-	-	-		9.53×10^{-05}	4.77×10^{-05}	1.91×10^{-04}	‡
0.580	0.488	0.690	-	-	-		5.66×10^{-05}	2.83×10^{-05}	1.13×10^{-04}	‡
0.822	0.691	0.977	-	-	-		3.18×10^{-05}	1.59×10^{-05}	6.35×10^{-05}	‡
1.162	0.977	1.382	-	-	-		1.85×10^{-05}	9.27×10^{-06}	3.71×10^{-05}	‡
1.64	1.38	1.95	5.07×10^{-08}	2.54×10^{-08}	1.01×10^{-07}	*	1.10×10^{-05}	5.52×10^{-06}	2.21×10^{-05}	‡
2.32	1.95	2.76	1.52×10^{-07}	9.65×10^{-08}	2.40×10^{-07}	*	6.26×10^{-06}	3.13×10^{-06}	1.25×10^{-05}	‡
3.28	2.76	3.90	3.55×10^{-07}	2.58×10^{-07}	4.89×10^{-07}	*	3.23×10^{-06}	1.62×10^{-06}	6.47×10^{-06}	‡
4.65	3.91	5.53	6.09×10^{-07}	4.72×10^{-07}	7.84×10^{-07}	*	1.55×10^{-06}	7.77×10^{-07}	3.11×10^{-06}	‡
6.56	5.52	7.81	5.07×10^{-07}	3.85×10^{-07}	6.68×10^{-07}	*	7.39×10^{-07}	3.69×10^{-07}	1.48×10^{-06}	‡
9.29	7.81	11.05	2.54×10^{-07}	1.75×10^{-07}	3.67×10^{-07}	*	3.48×10^{-07}	1.74×10^{-07}	6.95×10^{-07}	‡
13.08	11.00	15.56	1.53×10^{-07}	7.63×10^{-08}	3.05×10^{-07}	†	1.56×10^{-07}	7.78×10^{-08}	3.11×10^{-07}	‡
18.57	15.61	22.08	6.37×10^{-08}	3.18×10^{-08}	1.27×10^{-07}	†	6.37×10^{-08}	3.18×10^{-08}	1.27×10^{-07}	†
26.26	22.08	31.23	2.22×10^{-08}	1.11×10^{-08}	4.44×10^{-08}	†	2.22×10^{-08}	1.11×10^{-08}	4.44×10^{-08}	†
37.14	31.23	44.16	8.00×10^{-09}	4.00×10^{-09}	1.60×10^{-08}	†	8.00×10^{-09}	4.00×10^{-09}	1.60×10^{-08}	†
52.56	44.20	62.50	3.15×10^{-09}	1.57×10^{-09}	6.29×10^{-09}	†	3.15×10^{-09}	1.57×10^{-09}	6.29×10^{-09}	†
74.29	62.47	88.34	1.10×10^{-09}	5.50×10^{-10}	2.20×10^{-09}	†	1.10×10^{-09}	5.50×10^{-10}	2.20×10^{-09}	†
105.06	88.34	124.94	4.07×10^{-10}	2.03×10^{-10}	8.13×10^{-10}	†	4.07×10^{-10}	2.03×10^{-10}	8.13×10^{-10}	†
148.32	124.73	176.39	1.46×10^{-10}	7.28×10^{-11}	2.91×10^{-10}	†	1.46×10^{-10}	7.28×10^{-11}	2.91×10^{-10}	†

Table 1: The two models of present day cratering rates used in this study. Impact Model 1 is based on observed new small craters from Daubar et al. (2013) and Malin et al. (2006) combined with a rescaling of the 1 Gyr isochron of Hartmann (2005) for larger crater diameters and should be considered a lower bound on current impact rate. Impact Model 2 additionally incorporates modelling of smaller sub-observation scale impactors from Williams et al. (2014). Columns are: D crater diameter bin centre; D_1/D_2 minimum/maximum limits of crater diameter bin; N incremental cratering rate for each bin; N_{min}/N_{max} minimum/maximum cratering rate including all error contributions. Sources: *Daubar et al. (2013), error bar from Poisson statistics; † Hartmann (2005) 1 Gyr isochron scaled by 1/3 $\times10^{-9}$ to match Malin et al. (2006) and Daubar et al. (2013) observations, error bar standard factor of 2 error discussed in Hartmann (1999, 2005); ‡ modelling results from Williams et al. (2014) scaled to match the Daubar et al. (2013) crater counts in the 9.29 and 13.08 m bins. Bins are spaced by a factor of $\sqrt{2}$ and have the same bin centres as Hartmann (2005). Values are plotted in Figure 1.

Type	Source	Date (UT)	Time (UT)	Longitude (°E)	Latitude (°N)	Depth (m)	Yield (kg TNT)
Impact	Carancas Meteor Impact	15/09/2007	16:40:14	-69.044	-16.664	0.0	2000
	Apollo 14 LM	07/02/1971	00:45:25	-19.670	-3.420	0.0	778
	Apollo 16 SIVB	19/04/1972	21:02:04	-23.800	1.300	0.0	11000
	Apollo 17 SIVB	10/12/1972	20:32:42	-12.310	-4.210	0.0	11300
Explosion	EAGLE, SP11, Goha Tsion	11/01/2003	21:20:01	38.285	9.982	50.0	900
	EAGLE, SP12, Gerba Guracha	12/01/2003	21:20:00	38.476	9.759	50.0	1900
	EAGLE, SP13, Derba	13/01/2003	21:20:05	38.674	9.361	50.0	600
	EAGLE, SP14, Cheffe Donsa	12/01/2003	21:03:00	39.121	8.980	51.6	375
	EAGLE, SP16, Kula	13/01/2003	21:10:00	39.688	8.019	50.0	1100
	EAGLE, SP17, Bele	12/01/2003	21:10:00	40.032	7.727	50.0	2500
	EAGLE, SP18, Delo Sebro	11/01/2003	21:29:55	40.515	7.233	50.0	2200
	EAGLE, SP24, Koka	13/01/2003	21:50:00	39.005	8.328	51.5	525
	EAGLE, SP25, Doni B	12/01/2003	21:50:00	39.618	8.532	70.0	1025
	EAGLE, SP26, Beseka	14/01/2003	21:40:00	39.860	8.829	50.0	1150
	EAGLE, SP28, Gewane	11/01/2003	21:40:00	40.641	10.214	50.0	1000
	UK Nuclear Test, “Bristol”	26/11/1991	18:35:00	-116.070	37.096	457.0	11 000 000
	US Nuclear Test, “Divider”	23/09/1992	15:04:00	-115.989	37.021	426.0	5 000 000
	China Nuclear Test	29/07/1996	01:48:57	88.420	41.820	-	3 000 000
	DPRK Nuclear Test 1	09/10/2006	01:35:28	129.108	41.287	-	480 000
	DPRK Nuclear Test 3	12/02/2013	02:57:51	129.076	41.291	-	12 200 000

Table 2: Impact and explosive source parameters. Data compiled from: Carancas Impact (Brown et al., 2008; Le Pichon et al., 2008; Tancredi et al., 2009); Apollo Impacts (Toksoz et al., 1974; Williams, 2003); EAGLE chemical explosives (Maguire, 2003); UK/US nuclear tests (U. S. Department of Energy, 2000); Chinese nuclear test (Yang et al., 2003; CTBTO, 2012); and DPRK nuclear tests (Zhang and Wen, 2013).

Parameter	Value	Fractional Error	Notes
a_0	1.825×10^{-5}	2.45	Value for Earth fitted to explosion data in Figure 6
b	-1.60	0.023	Fitted to explosion data in Figure 6
c	0.5	-	Fixed (0.49±0.03 if fitted to data in Figure 6)
q	4.18×10^{6} J kg^{-1}	-	TNT yield (Shoemaker, 1983)
s	0.099	3.82	Fitted to impact data in Figure 6
a	5.568×10^{-5}	2.45	Value for Mars (eqn. 7)
$\alpha_\oplus$	8.8×10^{-3}	0.35	Teanby and Wookey (2011)
β	0.32	0.03	Teanby and Wookey (2011)
α	1.06×10^{-2}	0.35	Scaled to Mars gravity using eqn. 10
p_a	10^{-8} ms^{-2}Hz$^{-1/2}$	-	SEIS-SP power spectral density noise requirement
f_1, f_2	1, 16 Hz	-	Frequency range of regional events
f	4 Hz	-	Nominal frequency
p_v	4.0×10^{-10} ms^{-1}Hz$^{-1/2}$	-	From eqn. 13 and p_a
n_v	1.9×10^{-9} ms^{-1}	-	Peak velocity noise from eqn. 14
$g_\oplus$	9.81 ms^{-2}	-	Earth gravity
g	3.71 ms^{-2}	-	Mars gravity
r_{mars}	3 392 000 m	-	Mars radius

Table 3: Numerical values of parameters used to determine detectability of regional impacts. For impacts the overall uncertainty is dominated by the large errors in s and α.

Impact Model 1

Seismometer Noise ($ms^{-2}Hz^{-1/2}$)	Regional Impacts (<1200 km) N_{det} (yr^{-1})	1σ range (yr^{-1})	All Impacts (extrapolated) N_{det} (yr^{-1})	1σ range (yr^{-1})
1×10^{-7}	0.065	0.0055 – 0.77	0.065	0.0055 – 0.77
3×10^{-8}	0.28	0.025 – 3.3	0.29	0.025 – 3.4
1×10^{-8}	1.0	0.095 – 11	1.1	0.097 – 13
3×10^{-9}	3.3	0.39 – 34	5.0	0.43 – 57
1×10^{-9}	7.1	1.2 – 58	18	1.7 – 190

Impact Model 2

Seismometer Noise ($ms^{-2}Hz^{-1/2}$)	Regional Impacts (<1200 km) N_{det} (yr^{-1})	1σ range (yr^{-1})	All Impacts (extrapolated) N_{det} (yr^{-1})	1σ range (yr^{-1})
1×10^{-7}	0.17	0.015 – 2.1	0.17	0.015 – 2.1
3×10^{-8}	0.78	0.066 – 9.2	0.78	0.066 – 9.3
1×10^{-8}	2.9	0.26 – 34	3.1	0.26 – 37
3×10^{-9}	12	1.1 – 140	14	1.2 – 160
1×10^{-9}	40	4.1 – 450	52	4.6 – 600

Table 4: Number of detectable impacts N_{det} as a function of acceleration noise spectral density in the 1–16 Hz bandpass for the two impact models. A noise of 1×10^{-8} $ms^{-2}Hz^{-1/2}$ is the nominal SEIS-SP specification. For this and higher noise levels the majority of detectable impacts are regional, so there is minimal difference between the number of regional impacts detected and the extrapolated total number of impacts detected. For lower noise levels, impacts further away than 1200 km begin to make up a significant proportion of the detectable events.

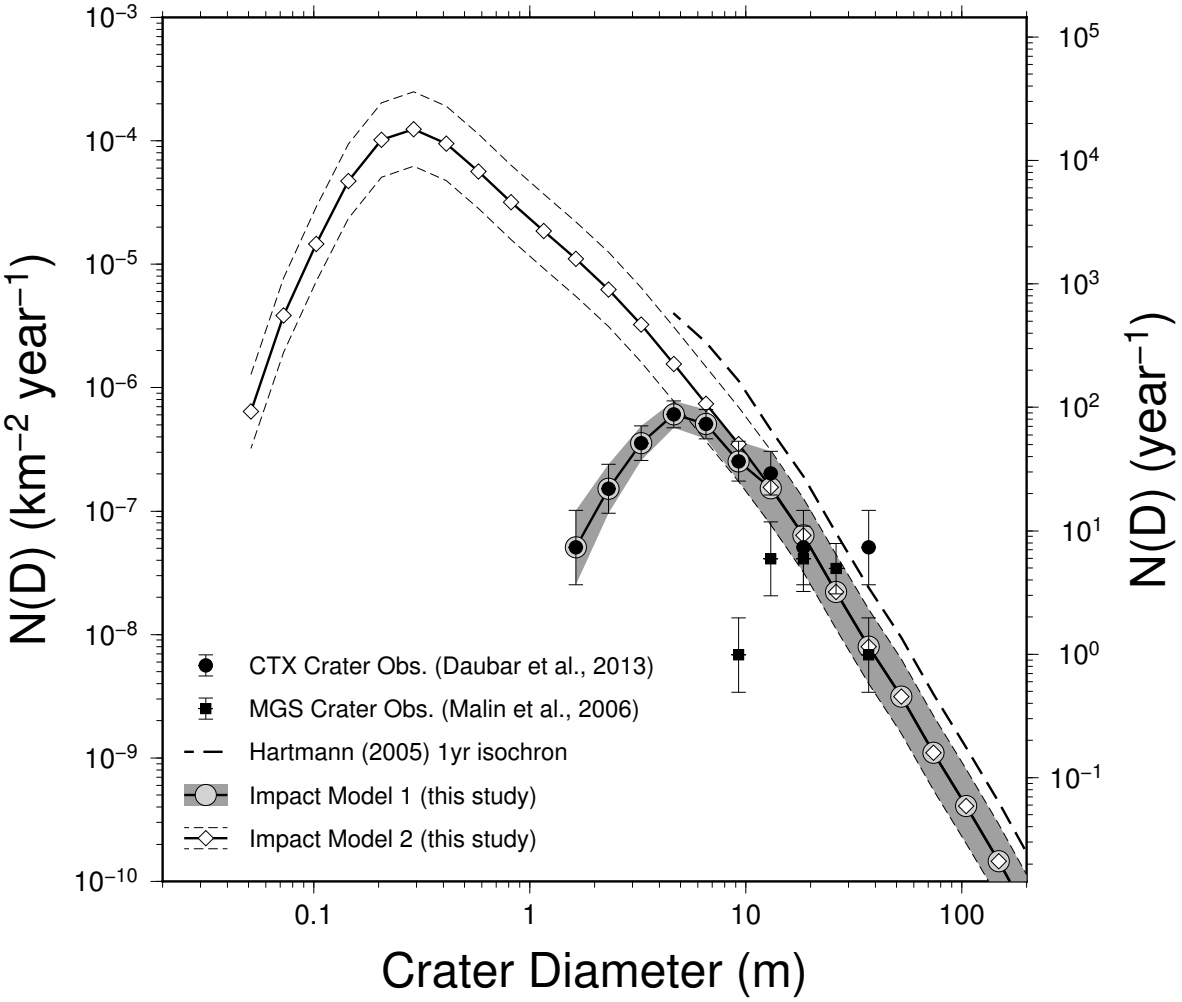

Figure 1: Current crater production function models and observations. $N(D)$ is the incremental number of craters in a bin centred on crater diameter D, with range $2^{-1/4}D$ to $2^{1/4}D$ (per km^2 on the left axis and for the whole of Mars for the right axis). Observations are from Malin et al. (2006) and Daubar et al. (2013). The downturn in $N(D)$ at small crater diameters in the new crater observations is attributed to finite image resolution or atmospheric ablation and deceleration. Values for the impact model curves are given in Table 1.

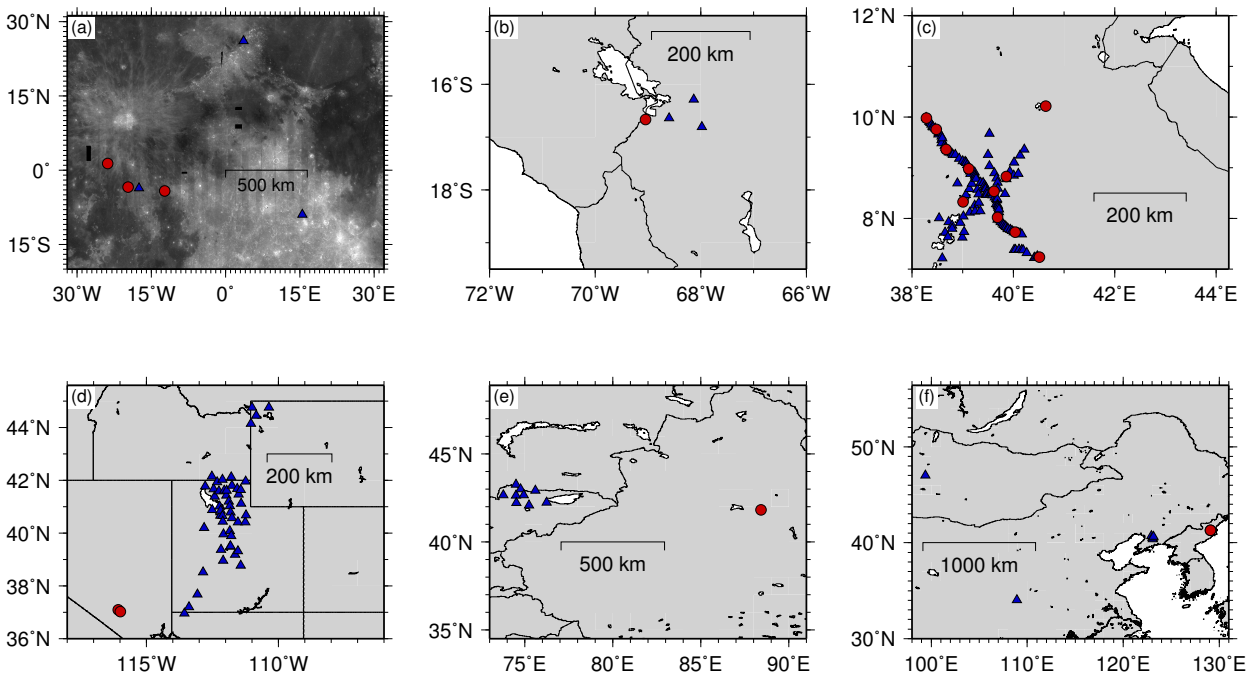

Figure 2: Location maps of impact and explosion datasets used to determine the distance-yield-amplitude scaling relation. Red circles are events (impacts or explosions) and blue triangles are seismometers. (a) Apollo artificial lunar impacts overlain on the Clementine lunar basemap. (b) Carancas impact event. (c) EAGLE controlled source chemical explosions. (d) US nuclear tests at the Nevada test site. (e) Chinese nuclear test. (f) North Korean nuclear tests.

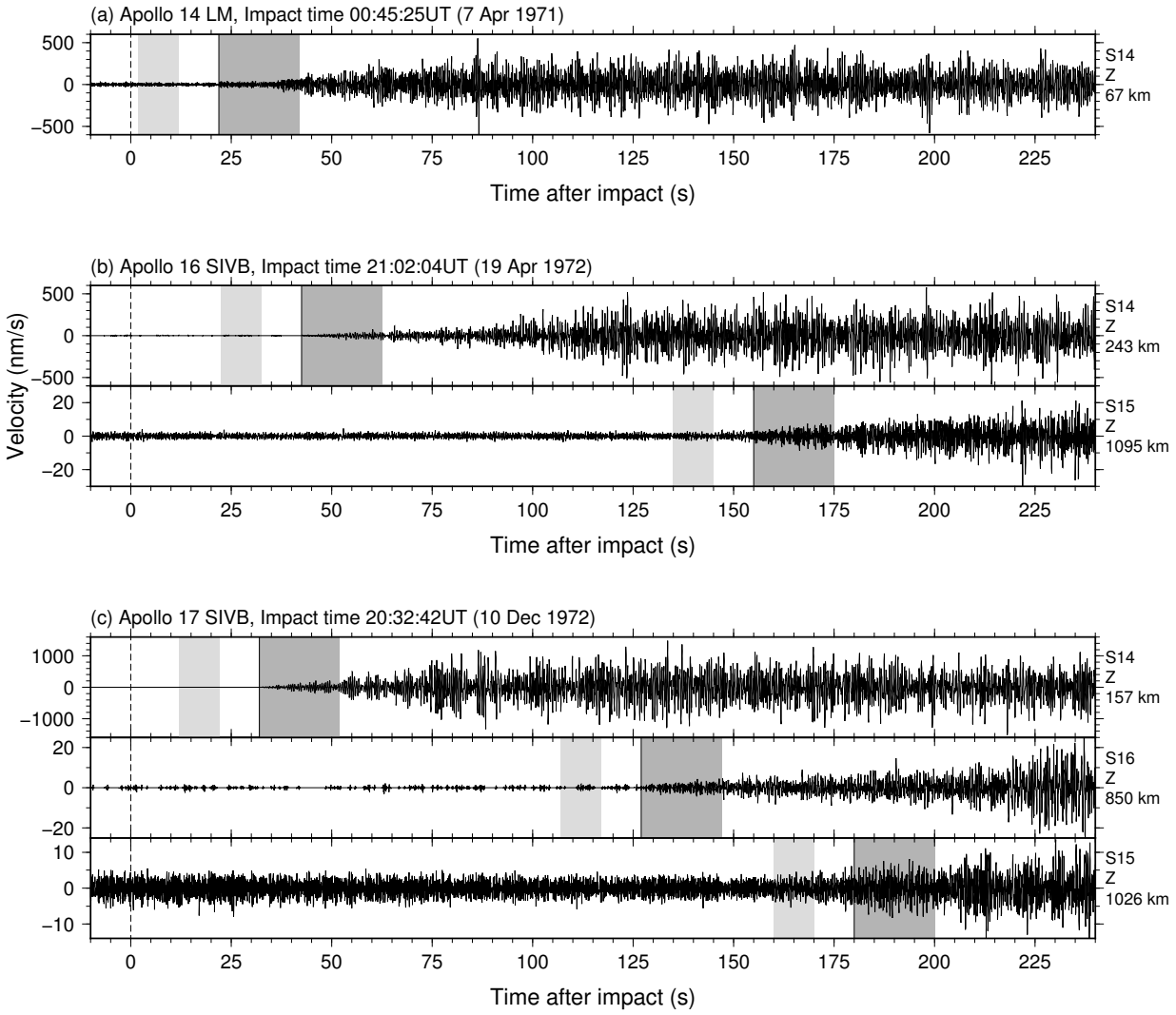

Figure 3: Seismic data from Apollo artificial impacts. (a) Apollo 14 lunar module (LM) impact recorded on the Apollo 14 seismometer. (b) Apollo 16 Saturn V booster stage (SIVB) recorded on Apollo 14 and 15 seismometers. (c) Apollo 17 SIVB recorded on Apollo 14, 15, and 16 seismometers. Vertical dashed line at 0 seconds indicates the impact time. Light grey region indicates noise window and dark grey window indicates first arrival window. Seismograms are from the short-period vertical sensor after deconvolution of the instrument response. Source-receiver distances shown on right of plot. Note the emergent nature of seismic events makes identification of a distinct first arrival phase difficult. Therefore, I used 20 seconds after the first arrival onset as a nominal first arrival window. Seismograms have been bandpass filtered between 1–16 Hz using a 4 pole Butterworth filter.

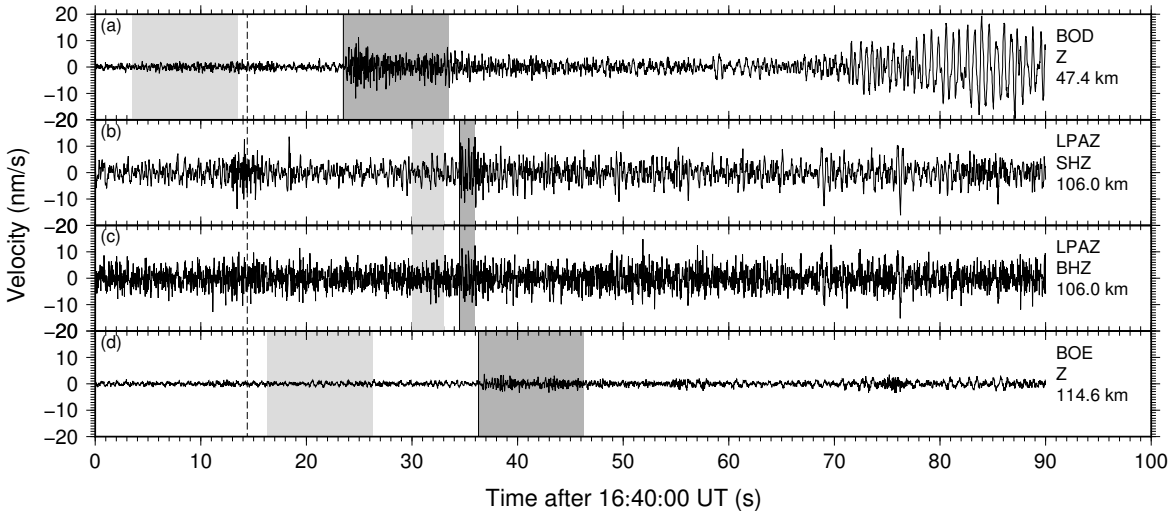

Figure 4: Seismic data from the Carancas impact event on 15^{th} September 2007. Vertical dashed lines indicate impact origin time (16:40:14 UT). Light grey region indicates noise window and dark grey window indicates first arrival window. (a) Short-period record from BSN station BOD. High amplitude arrival at >75 s is the airwave. (b,c) Short (SHZ) and long (BHZ) period records at GSN station LPAZ. Both instruments give comparable first arrival amplitudes. (d) short-period recording at BSN station BOE. All seismograms have been bandpass filtered using a 1–16 Hz 4 pole Butterworth filter.

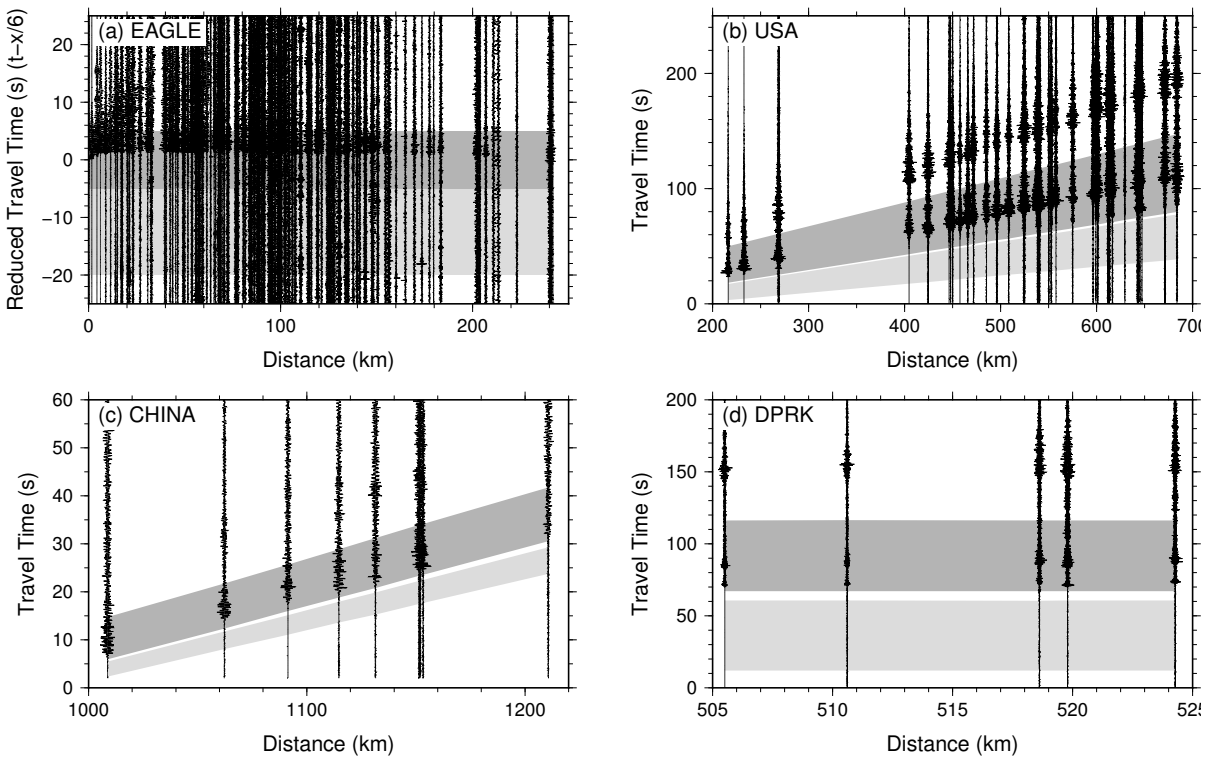

Figure 5: Example record sections from explosive data. (a) EAGLE shot point 14 at Cheffe Donsa, (b) US nuclear test "Divider", (c) Chinese 1996 nuclear test, and (d) DPRK 2006 nuclear test. Note that the EAGLE data in (a) is shown in reduced time relative to explosion origin time for clarity, whereas nuclear test data in (b,c,d) are in time relative to the reported explosion origin time. Light grey region indicates noise window and dark grey window indicates first arrival window. All seismograms have been bandpass filtered using a 1–16 Hz 4 pole Butterworth filter.

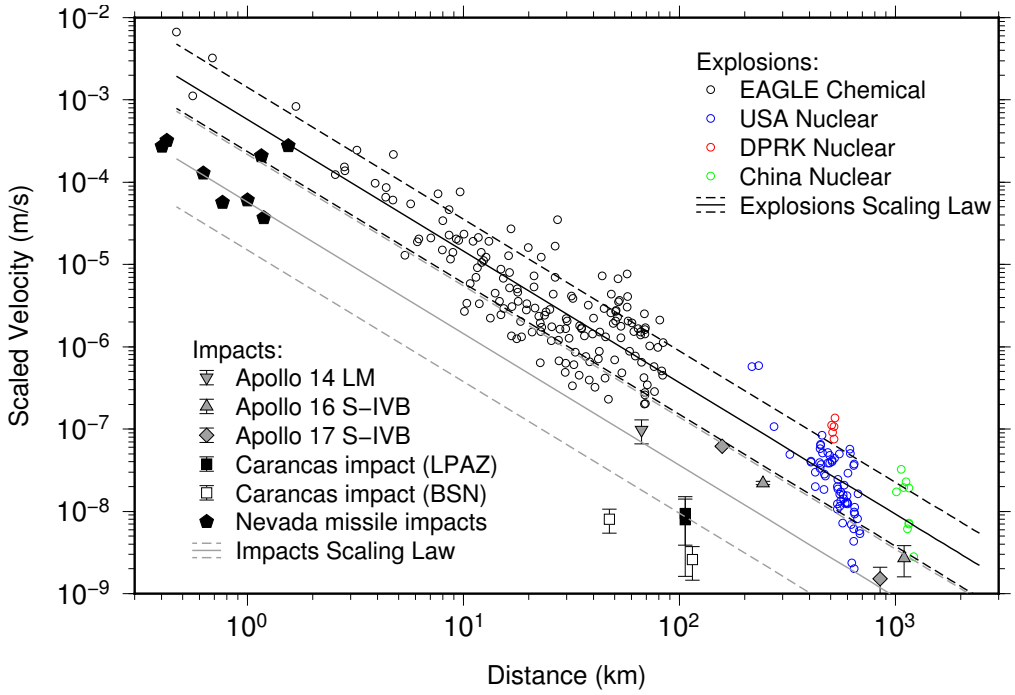

Figure 6: Peak seismogram amplitudes as a function of source-receiver distance from explosive and impact datasets. Solid lines show lines of best fit and dashed lines indicate 1σ uncertainties due to data scatter. Scaled velocity is the peak seismogram velocity in the first arrival window scaled by the square root of the yield as in equation 3 such that it is the equivalent peak seismogram velocity for a 1000 kg TNT event.

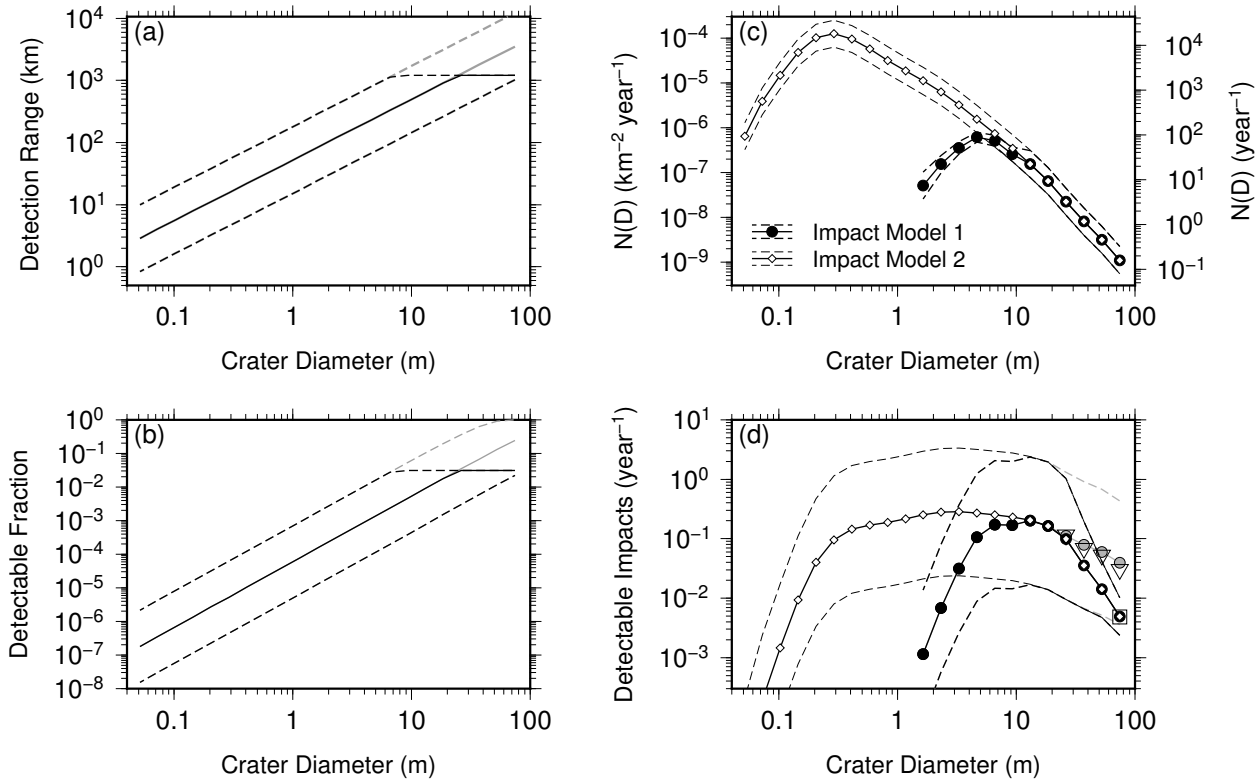

Figure 7: Detectability of regional impacts on Mars. (a) Maximum detection range of regional impacts as a function of crater diameter (black solid line) and associated 1σ uncertainties (black dashed lines). Impacts are only considered regional if they are within 1200 km of the seismometer, which is the range over which the peak amplitude scaling was determined. Hence, the detection range has a its maximum value set to 1200 km. Grey lines indicate an extrapolation of the scaling relation to greater source-receiver distances. (b) Detection range expressed as a proportion of Mars' surface. (c) Current crater production functions for impact models 1 and 2 along with 1-σ uncertainties (dashed lines). (d) Product of (b) and (c), which gives the number of detectable regional events (range <1200 km) per $\sqrt{2}$ diameter bin for impact model 1 (black circles) and impact model 2 (open diamonds). Dashed lines show 1-σ uncertainties for each model, which are dominated by the error in s (Table 3). Grey points indicate number of detections at all distances using the extrapolated scaling-relation. Open square at 74.29 m shows the prediction from Teanby and Wookey (2011) who assume a seismic efficiency k_s=2×10^{-5}. Open inverted triangles show re-calculated predictions from Teanby and Wookey (2011) assuming k_s=5×10^{-4}. This higher value of k_s gives much better agreement with predictions from the extrapolated scaling law. Note the model predictions from Teanby and Wookey (2011) also have an order of magnitude uncertainty, which is not shown for clarity.

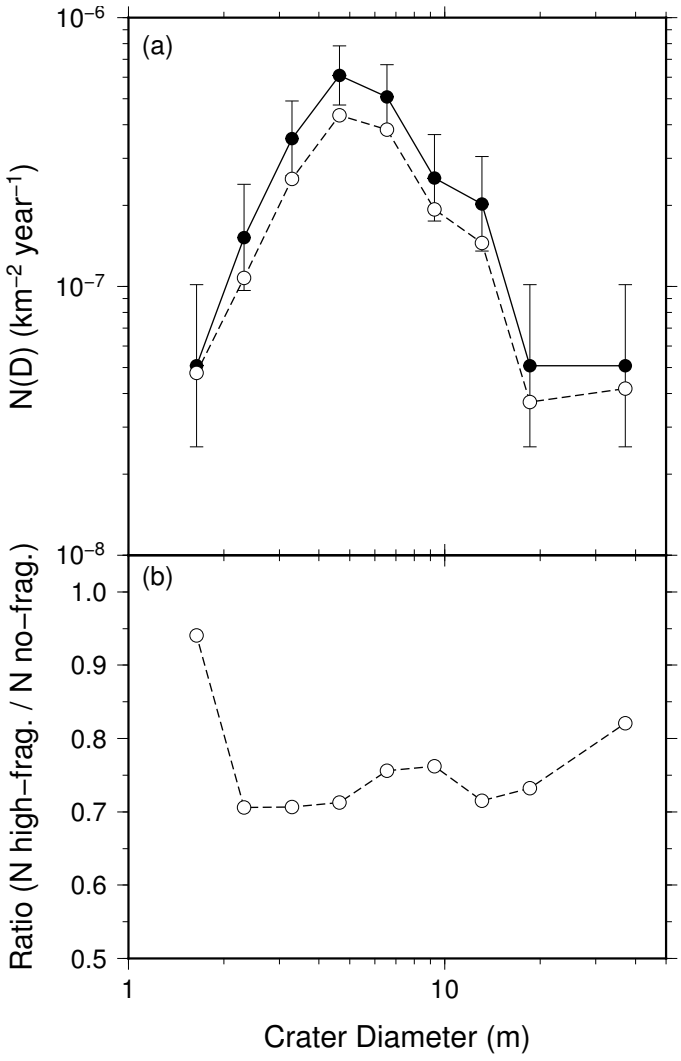

Figure 8: Effect of meteoroid fragmentation on number of observed craters. (a) Black circles with error-bars show the number of craters in each $\sqrt{2}$ crater diameter bin observed by Daubar et al. (2013), where clusters of craters assumed to be from the same meteoroid have been combined into a single effective crater diameter. Open circles show the number of individual craters predicted by mapping the observed crater numbers through the high fragmentation model of Williams et al. (2014). (b) Fragmentation causes a reduction in the formation rates of individual craters in the 2–40 m diameter range by a factor of ≈0.7. The effect of fragmentation is thus small compared to other error sources in this study.